

Event plane determination from the zero degree calorimeter at the Cooling Storage Ring external-target experiment*

Li-Ke Liu (<https://orcid.org/0000-0001-8052-483X>),¹ Hua Pei,¹ Ya-Ping Wang (<https://orcid.org/0000-0001-8573-6954>),¹
Biao Zhang (<https://orcid.org/0000-0001-6097-1878>),¹ Nu Xu,¹ and Shu-Su Shi^{1,†}

¹*Key Laboratory of Quark & Lepton Physics (MOE) and Institute of Particle Physics,
Central China Normal University, Wuhan 430079, China*

The Cooling Storage Ring external-target experiment (CEE) spectrometer is used to study the nuclear matter created in heavy-ion collisions at $\sqrt{s_{NN}} = 2.1\text{--}2.4$ GeV with the aim to reveal the quantum chromodynamics phase structure in the high-baryon density region. Collective flow is considered an effective probe for evaluating the properties of media during high-energy nuclear collisions. One of the main functions of the zero-degree calorimeter (ZDC), a subdetector system in the CEE, is to determine the reaction plane in heavy-ion collisions. This step is crucial for measuring the collective flow and other reaction-plane-related analyses. In this paper, we illustrate the procedures for event-plane determination using the ZDC. Finally, isospin-dependent quantum molecular dynamics model-based predictions of the rapidity dependence of the directed and elliptical flows for p , d , t , ^3He , and ^4He , produced in 2.1 GeV U+U collisions, are presented.

Keywords: QCD phase structure, Heavy-ion collisions, Collective flow, Reaction plane, Zero-Degree Calorimeter

I. INTRODUCTION

Quantum chromodynamics (QCD) predicts a phase transition from hadronic to deconfined partonic matter at sufficiently high temperatures and/or densities [1]. Results from top RHIC and LHC energies indicate that a new form of matter with a low viscosity and high temperature, quark-gluon plasma (QGP), has been produced [2–7]. Lattice QCD calculations predict that the phase transition from hadronic matter to the QGP phase is a smooth crossover in the vanishing baryon chemical potential (μ_B) region [8]. A first-order phase transition is expected in a finite baryon chemical potential region, and thus, determining the phase structure of the QCD is a major research goal in the field of medium- and high-energy heavy-ion collisions [9–12].

The Cooling Storage Ring external-target experiment (CEE) is a spectrometer that is employed to investigate the properties of nuclear matter in the 2.1–2.4 GeV energy region in the center-of-mass frame [13]. The CEE primarily allows near-full-space measurements of charged particles in heavy-ion collisions and provides experimental data for studying important scientific problems, such as spin- and isospin-related nuclear forces, nuclear matter equations of state, and QCD phase structures at high baryon number densities [14–16]. This offers valuable research opportunities for QCD phase diagram studies in low-temperature and high-baryon-density regions.

The event anisotropy of final-state particles relative to the reaction plane in momentum space, also known as collective

flow [17], is important for evaluating the properties of media created in heavy-ion collisions. Flow coefficients, such as directed flow v_1 and elliptical flow v_2 , are characterized by harmonic coefficients in the Fourier expansion of the azimuthal distribution of the final particles with respect to the reaction plane. In heavy-ion collisions, the driving force of the collective flow is the initial anisotropy in coordinate space. It rapidly diminishes as a function of time, and this phenomenon is known as the self-quenching effect. Thus, the collective flow is sensitive to the details of the expansion of nuclear matter during the early collision stage. The directed flow v_1 was predicted to be sensitive to the effective equation of state [18–20]. The elliptic flow v_2 is sensitive to the constituent interactions and degrees of freedom [21–23]. CEEs can reveal the collective flow in heavy-ion collisions at $\sqrt{s_{NN}} = 2.1\text{--}2.4$ GeV. This will help us study the medium properties and further search for possible QCD phase transition signals [24–26]. One of the principle functions of the zero-degree calorimeter (ZDC), a subdetector of the CEE, is to determine the reaction plane in nuclear-nuclear collisions. The reconstructed reaction plane (usually called the event plane) is crucial for many measurements, such as collective flow [27–29], azimuthal HBT [30], and CME-related observables [31–34].

In this paper, we introduce the necessary acceptance corrections and calibrations for event-plane determination from the CEE-ZDC. Furthermore, the isospin-dependent quantum molecular dynamics (IQMD) model [35] is used to predict collective flow from a typical CEE energy ($\sqrt{s_{NN}} = 2.1$ GeV).

II. CEE-ZDC

Figure 1(a) shows a schematic of the CEE spectrometer. The detector subsystem consists of a superconducting dipole magnet used to deflect charged particles; a silicon pixel positioning detector (SiPiX, Beam Monitor) to measure the position and time of the incident beam as well as the primary collision vertex [36]; A time projection chamber (TPC) is used

* This work was supported in part by the National Key Research and Development Program of China (Nos. 2022YFA1604900 and 2020YFE0202002), the National Natural Science Foundation of China (Nos. 12175084, 11890710, 11890711, 11927901), the Strategic Priority Research Program of the Chinese Academy of Sciences (No. XDB34030000), and Fundamental Research Funds for Central Universities (No. CCNU220N003).

† Corresponding author, shiss@mail.ccnu.edu.cn

to reconstruct particle trajectories and identify particles [37], and a time-of-flight chamber (TOF) is employed to extend particle identification to high momentums ($p > 2 \text{ GeV}/c$). The TOF chamber contains a start-time detector (T0) [38], an inner time-of-flight detector (iTof) [39], and an end-cap time-of-flight detector (eTOF) [40]. In addition, multi-wire drift chambers (MWDCs) are designed to track charged particles at forward rapidity and identify particles via momentum measurements [41]. The ZDC is used to measure the patterns (deposited energy and incident position) of forward-going charged particles emitted from nuclear–nuclear collisions [42].

The ZDC is proposed to be installed behind all the other subdetectors. The beam direction is defined as the positive Z -axis, and the ZDC is located at $Z = 295\text{--}299 \text{ cm}$, facing the original incident beam direction; its geometry is shown in Fig. 1(b). The ZDC detector cross-plane is a wheel with radius R ranging from 5 to 100 cm, and the vacuum pipe carrying the nuclear beam passes through the inner hole of this ZDC wheel. It consists of 24 sectors that subtend an azimuthal angle of 15° . Each sector is divided into eight modules forming eight rings in the full ZDC plane. The sensitive volume of the ZDC is composed of a plastic scintillator, and the current design uses the BC-408 material from Saint-Gobain [43]. The photons are produced inside the scintillator through the deposited energy of the incident particles and are then transported through a plastic light guide into the quartz window of a traditional PMT. ZDC covers the pseudo-rapidity range between 1.8 and 4.8, allowing the determination of the centrality and event plane in the forward rapidity region and minimizing autocorrelations from middle rapidity analyses [17, 44].

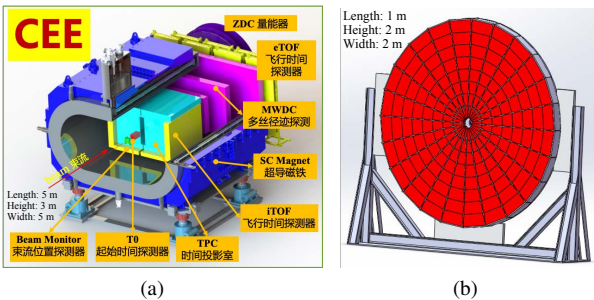


Fig. 1. (Color online) (a) Schematic of the CEE detector. (b) Schematic of the ZDC detector.

III. EVENT PLANE DETERMINATION FROM THE CEE-ZDC

In the study of the event plane, the simulation input of $^{238}\text{U} + ^{238}\text{U}$ collisions at 500 MeV/u was obtained from the IQMD generator [35]. The IQMD model was developed based on the quantum molecular dynamics (QMD) model [45] considering isospin effects. The detector environment was simulated using GEANT4 [46]. One million IQMD simulated events

were generated in the range of the nuclear impact parameter b , which is the transverse distance of the projectile from the target nucleus, $0 < b < 10 \text{ fm}$, with 0.1 million events for each b interval of 1 fm.

The reaction plane in the nucleus-nucleus collision is defined by the vector of the impact parameter and beam direction. As the impact parameter could not be directly measured in the experiment, the reaction plane was estimated using the standard event plane method [17, 47]. The first-order harmonic event plane Ψ_1 is calculated using the event flow vector \vec{Q}_1 :

$$\vec{Q}_1 = \left(\begin{array}{l} \sum_i w_i \sin(\phi_i) \\ \sum_i w_i \cos(\phi_i) \end{array} \right) \quad \Psi_1 = \tan^{-1} \left(\frac{\sum_i w_i \sin(\phi_i)}{\sum_i w_i \cos(\phi_i)} \right) \quad (1)$$

where the sum exceeds all particles used in the flow vector calculation. Quantities ϕ_i are the azimuths in the laboratory frame. The weight w_i is defined by the deposited energy ΔE of particle i collected by ZDC detector. As it is related to the mass and transverse momentum p_T of the particle, whereas the p_T weight is commonly applied in flow analysis to optimize the event plane resolution [47]. The smearing effect of the deposited energy is considered by Equ. 2

$$\begin{aligned} \Delta E &= \Delta E' * [1 - \frac{1}{4}(\frac{L}{5.5})^2], \quad h < 8 \\ \Delta E &= \Delta E' * [1 - \frac{1}{4}(\frac{L}{5.5})^2] * [8 + \frac{2}{3}(h - 8)], \quad h \geq 8 \end{aligned} \quad (2)$$

where L is the distance from the hit position to the geometric center of the sector. h is the charge of the final particle. The term $1 - \frac{1}{4}(\frac{L}{5.5})^2$ is used to describe the resolution of the deposited energy at the edge of the sector, and the term $8 + \frac{2}{3}(h - 8)$ is used to simulate the saturation effect of the deposited energy resolution for heavy nuclei ($h \geq 8$) [48].

Because the finite multiplicity limits the estimation of the reaction plane, it yields a resolution factor R which is defined by Equ. 3. In this study, we focus on the first-order harmonic event plane because v_1 is more significant than higher-order flows in the collision energy range covered by CEE.

$$R_1 = \langle \cos(\Psi_{1,EP} - \Psi_{1,RP}) \rangle \quad (3)$$

The magnetic field direction was perpendicular to the beam direction at CEE. Thus, the charged particles in the final state are deflected by the magnetic field and hit one side of the ZDC detector more, as shown in Fig. 2(a). Owing to the asymmetric ZDC acceptance, the reconstructed event-plane angle was not isotropic within the laboratory frame, but is biased towards the π -azimuth. The acceptance bias caused by the magnetic field introduces additional nonphysical anisotropy for the detected collision events, and this effect should be removed as it distorts the event plane reconstruction. Therefore, we introduce a position weight to calibrate asymmetric acceptance.

The core idea of the position weight is to correct the asymmetric acceptance of the ZDC caused by the magnetic field. Owing to the deflection of charged particles in the magnetic field, the left side of the ZDC detector receives more hits. We

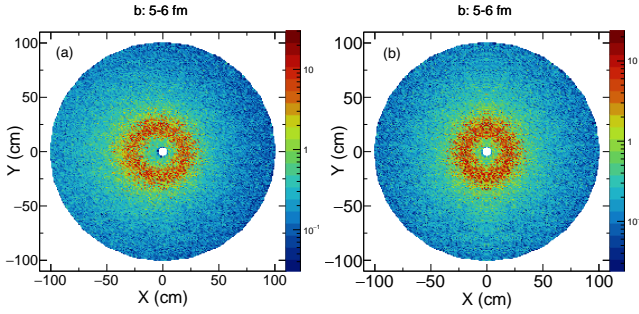


Fig. 2. (Color online) (a) Hit distribution obtained from the ZDC with a collision impact parameter of $5 < b < 6$ fm. (b) Hit distribution obtained from the ZDC after position weight correction with a collision impact parameter of $5 < b < 6$ fm.

assigned a weight P of less than 1 to the hits on the left side to correct this effect. The weight was calculated based on a two-dimensional $X - Y$ hit distribution, as defined in Eqn. 4 is the ratio of the number of hits on the right side to those on the left side. In addition, the deposited energy ΔE was used as the weight when calculating the number of hits. because it is related to particle mass. It can be observed that the acceptance of ZDC is symmetric after applying the position weight, as shown in Fig. 2(b).

$$\begin{aligned} w_i &= \Delta E \times P \\ P &= n(-x, y, \Delta E)/n(x, y, \Delta E), \quad x < 0 \\ P &= 1, \quad x > 0 \end{aligned} \quad (4)$$

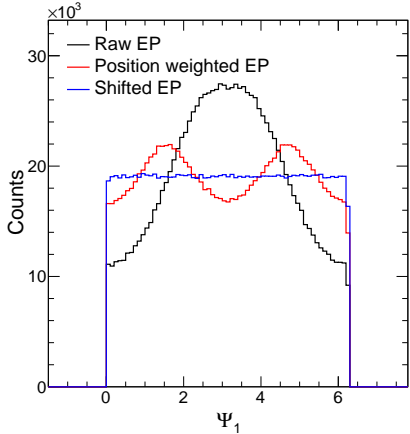


Fig. 3. (Color online) Event plane distributions before position weight correction (black line), after position weight correction (red line), and after position weight + shift corrections (blue line).

The black line in Fig. 3 shows the event plane distribution before position weight correction. With an ideal detector, the event plane distribution should be flat because the possible direction of the impact parameter b is random in the 2π azimuths of the transverse plane in the laboratory frame. It is not flat but peaks around $\Psi_1 \sim \pi$ owing to the asymmetric acceptance of ZDC as discussed above. Correspondingly, one can

see that the resolution difference between the left (azimuth of the reaction plane: $\pi/2$ to $3\pi/2$) and right sides ($-\pi/2$ to $\pi/2$) of ZDC is significant, as shown in Fig. 4(a). After applying the position weights defined in Eqn. 4: The unflatness of the event plane is significantly reduced, as indicated by the red line in Fig. 3. The resolution difference between the left and right sides of ZDC is significantly reduced, as shown in Fig. 4(b). This indicates that the position weight naturally corrected the acceptance asymmetry of ZDC.

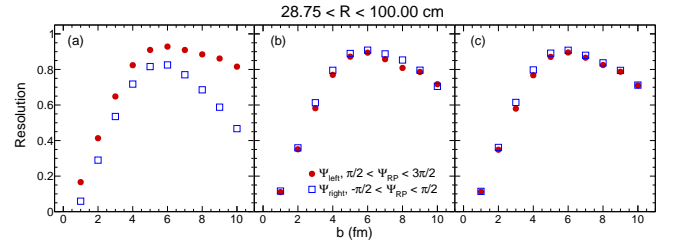


Fig. 4. (Color online) (a) Resolution of 1st order event plane as a function of impact parameter b without position weight. (b) Resolution of 1st order event plane as a function of b with position weight. (c) Resolution of 1st order event plane as a function of b with position weight and shift correction.

The event plane distribution is not perfectly flat after the position weight, as shown in Fig. 3. Consequently, the resolution difference between the left and right sides of ZDC was still visible. Therefore, the shift method is used to force the event plane to be flat [47]. A shift angle $\Delta\Psi_1$ is applied to correct the event plane. and $\Delta\Psi_1$ is calculated event-by-event using the following equation:

$$\begin{aligned} \Psi'_1 &= \Psi_1 + \Delta\Psi_1 \\ \Delta\Psi_1 &= \sum_{i=1}^{20} \frac{2}{i} [-\langle \sin(i\Psi_1) \rangle \cos(i\Psi_1) + \langle \cos(i\Psi_1) \rangle \sin(i\Psi_1)] \end{aligned} \quad (5)$$

where the brackets refer to the average over the events in the same centrality bins. Ψ_1 is the position-weight-corrected event plane azimuth, and Ψ'_1 is the event plane angle with shift calibration. After the shift calibration, a flat event plane distribution was achieved, as indicated by the blue line in Fig. 3. The resolution between the left and right sides was consistent, as shown in Fig. 4(c)).

In the experiment, the event plane calculated from different rapidity windows helped us understand the systematic uncertainties in the flow measurements. Correspondingly, the event planes from ZDC sub-rings, which correspond to different rapidity windows, were studied. Figure 5 shows the 1st order event plane resolution from ZDC sub-ring radius $52.5 < R < 76.25$ cm without a position weight 5(a), with a position weight 5(,) and with a position weight and shift correction 5(c). These results indicate that the position weight and shift methods work well for the event plane calculated by ZDC subring.

After eliminating the resolution difference due to asymmetric acceptance using the position weight and shift methods, the 1st-order event plane resolution from the ZDC was

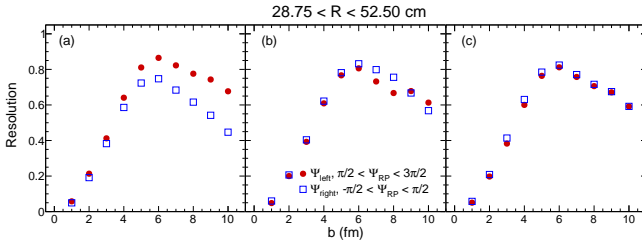


Fig. 5. (Color online) (a) Resolution of 1st order event plane, determined from the ZDC sub-ring (radius: $52.5 < R < 76.25$ cm) without position weight. (b) Resolution of 1st order event plane, determined from the ZDC sub-ring (radius: $52.5 < R < 76.25$ cm) with position weight. (c) Resolution of 1st order event plane, determined from the ZDC sub-ring (radius: $52.5 < R < 76.25$ cm) with position weight and shift corrections.

calculated using the two-sub-event plane method [17]. The full event was divided randomly into two independent sub-events with equal tracks, and the event-plane resolution was estimated by correlating the two sub-events. as defined by Eq. 6:

$$\begin{aligned} R_{1,\text{sub}} &= \sqrt{\langle \cos(\Psi_1^A - \Psi_1^B) \rangle} \\ &= \sqrt{\pi}/2\chi e^{(-\chi^2/2)} (I_0(\chi^2/2) + I_1(\chi^2/2)) \end{aligned} \quad (6)$$

where A and B denote the two subevents. As χ is proportional to the square root of the multiplicity and a full event with two particles as subevents, The full event-plane resolution is obtained as follows:

$$R_{\text{full}} = R \left(\sqrt{2}\chi_{\text{sub}} \right) \quad (7)$$

The resolution of 1st-order event plane as a function of impact parameter, determined from the ZDC whole ring, is compared with the 1st-order event plane resolution, determined from the STAR event plane detector, for Au+Au collisions at $\sqrt{s_{\text{NN}}} = 3.0$ GeV [28] in Fig. 6. The event plane resolution from CEE-ZDC reached $\sim 90\%$ in the middle-central collisions ($4 < b < 7$ fm). The resolution of ZDC is better in the region of $b < 4$ fm but worse for $b > 4$ fm, which is probably due to the different sizes of the gold and uranium nuclei, experimental acceptance, and detector performance.

We also systematically investigated the effects of the ZDC detector thickness, hit efficiency, energy resolution, and model dependence on the first-order event plane resolution. As shown in Fig. 7, where the solid red dots represent the default conditions: a ZDC thickness of 4 cm, hit efficiency of 100%, and default energy smearing, as shown in Eq. 2 and heavy nuclei from IQMD generator de-excitation. The effects of the different variables were investigated individually. The resolution of 1st-order event plane decreases slightly as the ZDC detector thickness decreases, as shown in Fig. 7(a). This is because a more accurate measurement of the deposited energy is achieved with a thicker ZDC. Fig. 7(b) shows the hit efficiency dependence of 1st-order event-plane resolution. The ZDC hit efficiency was reduced to 90%, and

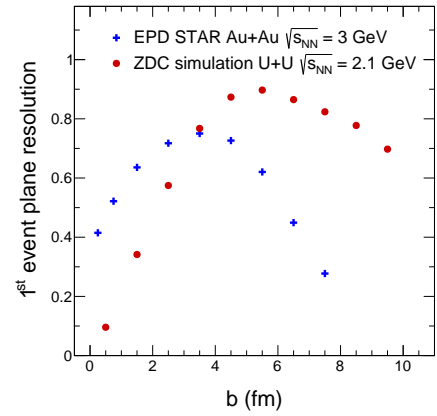


Fig. 6. (Color online) Resolution of 1st order event plane, determined from the ZDC whole ring, as a function of impact parameter compared with that of 1st order event plane determined from STAR event plane detector for Au+Au collisions at $\sqrt{s_{\text{NN}}} = 3.0$ GeV.

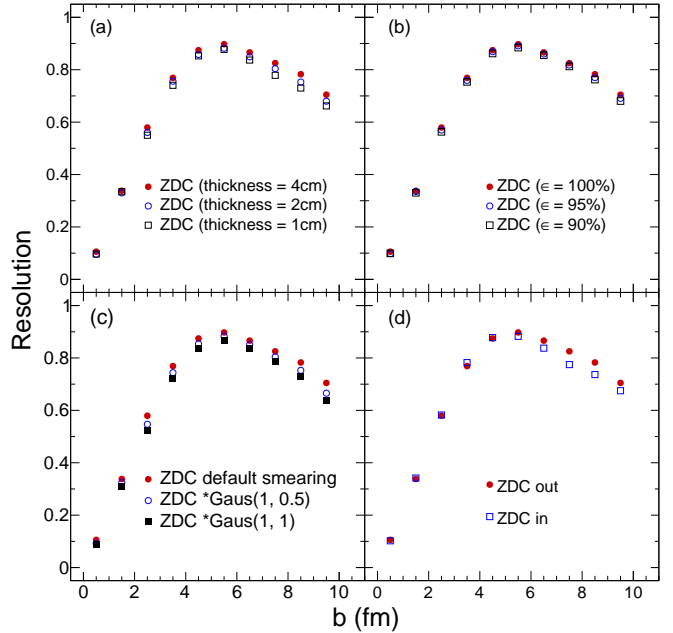


Fig. 7. (Color online) (a) Effect of ZDC thickness on the 1st order event plane resolution. (b)Effect of ZDC hit efficiency on the 1st order event plane resolution. (c)Effect of ZDC energy resolution on the 1st order event plane resolution. (d)Effect of heavy nuclei de-excitation on the 1st order event plane resolution.

the event-plane resolution remained almost unchanged. The effect of ZDC energy resolution is investigated by applying additional Gaussian smearing to the deposited energy, where Gaussian(1, 0.5) has a center value of 1 and width of 0.5, and Gaussian(1, 1) has a center value of 1 and width of 1. A smaller Gaussian width indicates a better energy resolution. As the energy resolution decreases, the first-order event-plane

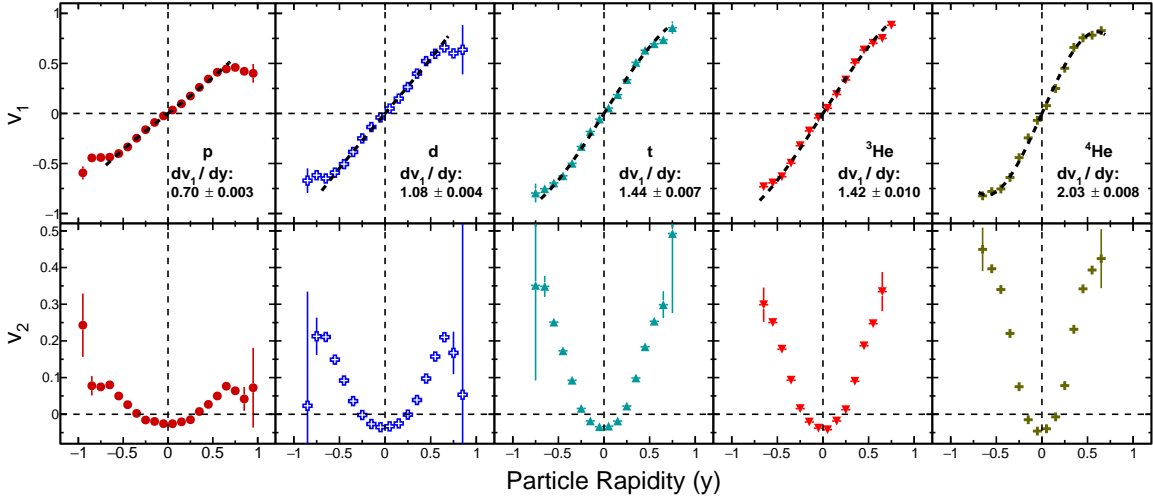


Fig. 8. (Color online) v_1 and v_2 as functions of rapidity, for protons, deuterons, tritons, ${}^3\text{He}$, and ${}^4\text{He}$ with a collision impact parameter $1 < b < 4 \text{ fm}$, derived from IQMD ${}^{238}\text{U} + {}^{238}\text{U}$ 500 MeV/u ($\sqrt{s_{\text{NN}}} = 2.1 \text{ GeV}$). The v_1 slopes are extracted using the equation: $y = ax + bx^3$.

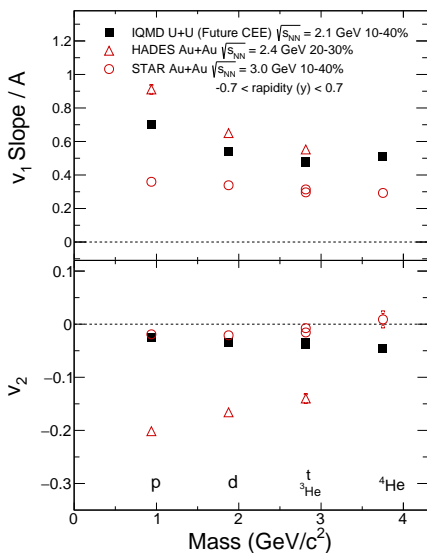


Fig. 9. (Color online) Atomic number A scaled v_1 slope (upper panel) and v_2 (lower panel) at middle rapidity for protons, deuterons, tritons, ${}^3\text{He}$, and ${}^4\text{He}$ determined from HADES, STAR experiments, and IQMD model calculations for CEE. The brackets represent the systematic uncertainties in the experimental data.

resolution decreases by approximately 5-10%, as shown in Fig. 7(c). Figure 7(d) shows the relationship between the ZDC event plane resolution and the IQMD heavy nuclei de-excitation, where "out"/"in" means the heavy nuclei are de-excitation or not. The resolution estimated using the IQMD model with heavy nuclei de-excitation was slightly higher than IQMD without heavy nuclei de-excitation because the multiplicity was higher in the former case.

IV. COLLECTIVITY FLOW PREDICTIONS FROM IQMD MODEL

Collective flow is sensitive to the details of the expansion of the medium produced during the early collision stage. Flow measurements at CEE provide information on the QCD phase structure in the high-baryon-density region. Collectivity flow predictions were presented for a typical CEE based on IQMD model. Figure 8 shows v_1 and v_2 as functions of rapidity for protons, deuterons, tritons, ${}^3\text{He}$, and ${}^4\text{He}$ with an impact parameter of $1 < b < 4 \text{ fm}$ from IQMD ${}^{238}\text{U} + {}^{238}\text{U}$ collisions at 500 MeV/u ($\sqrt{s_{\text{NN}}} = 2.1 \text{ GeV}$). The v_1 slope values extracted using $y = ax + bx^3$ strongly depend on the number of nuclei. The v_2 values are negative in the middle rapidity owing to the squeeze-out effect; the medium expansion is shadowed by spectator nucleons, and particles are preferentially emitted in the direction perpendicular to the reaction plane [17], whereas v_2 becomes positive in the forward rapidity as the squeeze-out effect becomes weak. Similar to v_1 slope, v_2 values showed a strong dependence on the number of nuclei.

Figure 9 presents the $d(v_1/A)/dy$ and v_2 for protons, deuterons, tritons, ${}^3\text{He}$, and ${}^4\text{He}$ determined from HADES [49] and STAR [50] experiments together with the IQMD model calculations ³, where A denotes the atomic number. v_1/A represents the directed flow carried by each nucleon in the light nuclei, and the scaling behavior suggests a coalescence production mechanism of the light nuclei during heavy-ion collisions. v_2 is calculated in the rapidity range of $-0.1 < y < 0$ for the STAR experiment and IQMD model calculations and $-0.05 < y < 0.05$ for the HADES experiment. The atomic-number-scaled v_1 slope from HADES and

³ Unlike in the experiment, the centrality here is determined from the impact parameter in the model calculations.

IQMD showed a decreasing trend with an increase in atomic number, whereas the STAR data weakly depend on the atomic number in the collisions at $\sqrt{s_{NN}} = 3$ GeV. The absolute value of v_2 from HADES decreased with increasing atomic number, whereas the results for STAR and IQMD remained almost unchanged with atomic number. This may indicate that light nuclei are not purely formed by the coalescence mechanism in Au+Au collisions at $\sqrt{s_{NN}} = 2.4$ GeV. Coalescence was the dominant production mechanism for Au+Au $\sqrt{s_{NN}} = 3.0$ GeV. The production of light nuclei in the IQMD model is a mixture of light nuclei fragments and the coalescence of nucleons and light nuclei. The dominant production mechanism in the IQMD model depends on the collision energy and parameter settings. The predictions provided by the IQMD model in U + U collisions at $\sqrt{s_{NN}} = 2.1$ GeV will be validated in future CEEs.

Future measurements of v_1 and v_2 will help us to examine the equation of state of the produced nuclear matter at CEE energies [51, 52] and understand the production mechanism of light nuclei in the high baryon density region [15, 53–56].

V. SUMMARY

In this paper, we elucidate the procedures for event plane determination from the ZDC at the CEE. The calculated values determined using the IQMD Monte Carlo event generator (500 MeV/u ^{238}U + ^{238}U) were incorporated as inputs, and the detector environment was simulated using GEANT4.

To correct for the bias caused by the dipole magnet, a position-dependent weight was introduced to calibrate the asymmetric acceptance. After an additional shift correction, an outstanding first-order event plane resolution of $\sim 90\%$ was obtained for middle-central collisions ($4 < b < 7$ fm). Herein, the collective flows v_1 and v_2 , as functions of rapidity for p , d , t , ^3He , and ^4He in middle central collisions, are pre-

sented based on the IQMD model. These results were compared with the experimental data obtained from 2.4 GeV and 3 GeV Au+Au collisions in the HADES and STAR experiments, respectively.

The measurements from the HADES and STAR experiments suggest that coalescence is the dominant production mechanism of light nuclei at 3 GeV, whereas light nuclei fragmentation and coalescence are both important at 2.4 GeV. The predictions of the IQMD model at 2.1 GeV will be validated in future CEEs.

ACKNOWLEDGMENTS

We thank Prof. Li Ou and Zhigang Xiao for generating the IQMD data and for fruitful discussions.

AUTHOR CONTRIBUTIONS

All authors contributed to the study conception and design, material preparation, data collection and analysis. The first draft of the manuscript was written by Li-Ke Liu and Shu-Su Shi, and all authors commented on previous versions of the manuscript. All authors read and approved the final manuscript.

DATA AVAILABILITY STATEMENT

The data that support the findings of this study are openly available in Science Data Bank at <https://doi.org/10.57760/scencedb.09132> and <https://cstr.cn/31253.11.scencedb.09132>.

-
- [1] P. B. Munzinger and J. Stachel, The quest for the quark-gluon plasma. *Nature* **448**, 302-309 (2007). doi: [10.1038/nature06080](https://doi.org/10.1038/nature06080)
 - [2] I. Arsene *et al.*, Quark gluon plasma and color glass condensate at RHIC? Perspective of the BRAHMS experiment. *Nucl. Phys. A* **757**, 1-27 (2005). doi: [10.1016/j.nuclphysa.2005.02.130](https://doi.org/10.1016/j.nuclphysa.2005.02.130)
 - [3] B. B. Back *et al.*, The PHOBOS perspective on discoveries at RHIC. *Nucl. Phys. A* **757**, 28-101 (2005). doi: [10.1016/j.nuclphysa.2005.03.084](https://doi.org/10.1016/j.nuclphysa.2005.03.084)
 - [4] K. Adcox *et al.*, Formation of dense partonic matter in relativistic nucleus-nucleus collisions at RHIC: Experimental evaluation by the PHENIX collaboration. *Nucl. Phys. A* **757**, 184-283 (2005). doi: [10.1016/j.nuclphysa.2005.03.086](https://doi.org/10.1016/j.nuclphysa.2005.03.086)
 - [5] J. Adams *et al.*, Experimental and theoretical challenges in the search for the quark gluon plasma: The STAR Collaboration's critical assessment of the evidence from RHIC collisions. *Nucl. Phys. A* **757**, 102-183 (2005). doi: [10.1016/j.nuclphysa.2005.03.085](https://doi.org/10.1016/j.nuclphysa.2005.03.085)
 - [6] A. Bazavov *et al.*, The chiral and deconfinement aspects of the QCD transition. *Phys. Rev. D* **85**, 054503 (2012). doi: [10.1103/PhysRevD.85.054503](https://doi.org/10.1103/PhysRevD.85.054503)
 - [7] K. Fukushima and C. Sasaki, The phase diagram of nuclear and quark matter at high baryon density. *Prog. Part. Nucl. Phys.* **72**, 99-154 (2013). doi: [10.1016/j.ppnp.2013.05.003](https://doi.org/10.1016/j.ppnp.2013.05.003)
 - [8] Y. Aoki, G. Endrodi, Z. Fodor *et al.*, The Order of the quantum chromodynamics transition predicted by the standard model of particle physics. *Nature* **443**, 675-678 (2006). doi: [10.1038/nature05120](https://doi.org/10.1038/nature05120)
 - [9] K. Fukushima and T. Hatsuda, The phase diagram of dense QCD. *Rept. Prog. Phys.* **74**, 014001 (2011). doi: [10.1088/0034-4885/74/1/014001](https://doi.org/10.1088/0034-4885/74/1/014001)
 - [10] A. Bzdak *et al.*, Mapping the phases of quantum chromodynamics with beam energy scan. *Phys. Rept.* **853**, 1-87 (2020). doi: [10.1016/j.physrep.2020.01.005](https://doi.org/10.1016/j.physrep.2020.01.005)
 - [11] X. Luo, S. Shi, N. Xu *et al.*, A study of the properties of the QCD phase diagram in high-energy nuclear collisions. *Particle* **3**(2), 278-307 (2020). doi: [10.3390/particles3020022](https://doi.org/10.3390/particles3020022)

- [12] H. Huang *et al.*, Collective excitation in high-energy nuclear collisions – In memory of professor Lianshou Liu. *Symmetry* **15** 499 (2023). doi: [10.3390/sym15020499](https://doi.org/10.3390/sym15020499)
- [13] L. Lü *et al.*, Conceptual design of the HIRFL-CSR external-target experiment. *Sci. China Phys. Mech. Astron.* **60**(1), 012021 (2017). doi: [10.1007/s11433-016-0342-x](https://doi.org/10.1007/s11433-016-0342-x)
- [14] C. J. Horowitz *et al.*, A way forward in the study of the symmetry energy: experiment, theory, and observation. *J. Phys. G* **41**, 093001 (2014). doi: [10.1088/0954-3899/41/9/093001](https://doi.org/10.1088/0954-3899/41/9/093001)
- [15] S. Zhang *et al.*, Searching for onset of deconfinement via hypernuclei and baryon-strangeness correlations. *Phys. Lett. B* **684**, 224-227 (2010). doi: [10.1016/j.physletb.2010.01.034](https://doi.org/10.1016/j.physletb.2010.01.034)
- [16] A. Andronic *et al.*, Hadron production in ultra-relativistic nuclear collisions: Quarkyonic matter and a triple point in the phase diagram of QCD. *Nucl. Phys. A* **837**, 65-86 (2010). doi: [10.1016/j.nuclphysa.2010.02.005](https://doi.org/10.1016/j.nuclphysa.2010.02.005)
- [17] S. A. Voloshin, A. M. Poskanzer, R. Snellings, Collective phenomena in non-central nuclear collisions. *Landolt-Bornstein*. **23**, 293-333 (2010). doi: [10.1007/978-3-642-01539-7_10](https://doi.org/10.1007/978-3-642-01539-7_10)
- [18] S. A. Bass *et al.*, Microscopic models for ultrarelativistic heavy ion collisions. *Prog. Part. Nucl. Phys.* **41**, 255-369 (1998). doi: [10.1016/S0146-6410\(98\)00058-1](https://doi.org/10.1016/S0146-6410(98)00058-1)
- [19] J. Steinheimer *et al.*, The high-density equation of state in heavy-ion collisions: constraints from proton flow. *Eur. Phys. J. C* **82**(10), 911 (2022). doi: [10.1140/epjc/s10052-022-10894-w](https://doi.org/10.1140/epjc/s10052-022-10894-w)
- [20] D. Oliinychenko, A. Sorensen, V. Koch *et al.*, Sensitivity of Au+Au collisions to the symmetric nuclear matter equation of state at 2 – 5 nuclear saturation densities. arXiv:2208.11996
- [21] L. Adamczyk *et al.*, Centrality and transverse momentum dependence of elliptic flow of multistrange hadrons and ϕ meson in Au+Au collisions at $\sqrt{s_{\text{NN}}} = 200$ GeV. *Phys. Rev. Lett.* **116**(6), 062301 (2016). doi: [10.1103/PhysRevLett.116.062301](https://doi.org/10.1103/PhysRevLett.116.062301)
- [22] L. Adamczyk *et al.*, Measurement of D^0 azimuthal anisotropy at midrapidity in Au+Au collisions at $\sqrt{s_{\text{NN}}} = 200$ GeV. *Phys. Rev. Lett.* **118**(21), 212301 (2017). doi: [10.1103/PhysRevLett.118.212301](https://doi.org/10.1103/PhysRevLett.118.212301)
- [23] S. Shi, An experimental review on elliptic flow of strange and multistrange hadrons in relativistic heavy ion collisions. *Adv. High Energy Phys.* **2016**, 1987432 (2016). doi: [10.1155/2016/1987432](https://doi.org/10.1155/2016/1987432)
- [24] Y. Nara and A. Ohnishi, Mean-field update in the JAM microscopic transport model: Mean-field effects on collective flow in high-energy heavy-ion collisions at $\sqrt{s_{\text{NN}}} = 2-20$ GeV energies. *Phys. Rev. C* **105**(1), 014911 (2022). doi: [10.1103/PhysRevC.105.014911](https://doi.org/10.1103/PhysRevC.105.014911)
- [25] Y. Nara, A. Jinno, K. Murase *et al.*, Directed flow of Λ in high-energy heavy-ion collisions and Λ potential in dense nuclear matter. *Phys. Rev. C* **106**(4), 044902 (2022). doi: [10.1103/PhysRevC.106.044902](https://doi.org/10.1103/PhysRevC.106.044902)
- [26] S. Lan and S. Shi, Anisotropic flow in high baryon density region. *Nucl. Sci. Tech.* **33**(3), 21 (2022). doi: [10.1007/s41365-022-01006-0](https://doi.org/10.1007/s41365-022-01006-0)
- [27] L. Adamczyk *et al.*, Beam-energy dependence of the directed flow of protons, antiprotons, and pions in Au+Au collisions. *Phys. Rev. Lett.* **112**(16) 162301 (2014). doi: [10.1103/PhysRevLett.112.162301](https://doi.org/10.1103/PhysRevLett.112.162301)
- [28] M. S. Abdallah *et al.*, Disappearance of partonic collectivity in $\sqrt{s_{\text{NN}}} = 3$ GeV Au+Au collisions at RHIC. *Phys. Lett. B* **827**, 137003 (2022). doi: [10.1016/j.physletb.2022.137003](https://doi.org/10.1016/j.physletb.2022.137003)
- [29] Y. Nara *et al.*, Dynamical evolution of heavy-ion collisions. doi: [10.1007/978-981-19-4441-3_3](https://doi.org/10.1007/978-981-19-4441-3_3)
- [30] L. Adamczyk *et al.*, Beam-energy-dependent two-pion interferometry and the freeze-out eccentricity of pions measured in heavy ion collisions at the star detector. *Phys. Rev. C* **92** 014904 (2015). doi: [10.1103/PhysRevC.92.014904](https://doi.org/10.1103/PhysRevC.92.014904)
- [31] Fukushima *et al.*, The chiral magnetic effect. *Phys. Rev. D* **78**, 074033 (2008). doi: [10.1103/PhysRevD.78.074033](https://doi.org/10.1103/PhysRevD.78.074033)
- [32] L. Adamczyk *et al.*, Search for the chiral magnetic effect via charge-dependent azimuthal correlations relative to spectator and participant planes in Au + Au collisions at $\sqrt{s_{\text{NN}}} = 200$ GeV. *Phys. Rev. Lett.* **128**, 092301 (2022). doi: [10.1103/PhysRevLett.128.092301](https://doi.org/10.1103/PhysRevLett.128.092301)
- [33] X. Zhao, G. Ma, Search for the chiral magnetic effect in collisions between two isobars with deformed and neutron-rich nuclear structures. *Phys. Rev. C* **106**(3), 034909 (2022). doi: [10.1103/PhysRevC.106.034909](https://doi.org/10.1103/PhysRevC.106.034909)
- [34] B. Chen, X. Zhao, G. Ma, On the difference between signal and background of the chiral magnetic effect relative to spectator and participant planes in isobar collisions at $\sqrt{s_{\text{NN}}} = 200$ GeV. arXiv:2301.12076
- [35] C. Hartnack *et al.*, Modeling the many body dynamics of heavy ion collisions: Present status and future perspective. *Eur. Phys. J. A* **1**, 151-169 (1998). doi: [10.1007/s100500050045](https://doi.org/10.1007/s100500050045)
- [36] H. Wang *et al.*, Design and tests of the prototype a beam monitor of the CSR external target experiment. *Nucl. Sci. Tech.* **33**(3), 36 (2022). doi: [10.1007/s41365-022-01021-1](https://doi.org/10.1007/s41365-022-01021-1)
- [37] W. Huang *et al.*, Laser test of the prototype of CEE time projection chamber. *Nucl. Sci. Tech.*, **29**(3), 41 (2018). doi: [10.1007/s41365-018-0382-4](https://doi.org/10.1007/s41365-018-0382-4)
- [38] D. Hu *et al.*, Extensive beam test study of prototype MRPCs for the T0 detector at the CSR external-target experiment. *Eur. Phys. J. C* **80**(3), 282 (2020). doi: [10.1140/epjc/s10052-020-7804-2](https://doi.org/10.1140/epjc/s10052-020-7804-2)
- [39] X. Wang *et al.*, CEE inner TOF prototype design and preliminary test results. *JINST* **17**(09), P09023 (2022). doi: [10.1088/1748-0221/17/09/P09023](https://doi.org/10.1088/1748-0221/17/09/P09023)
- [40] B. Wang *et al.*, The CEE-eTOF wall constructed with new sealed MRPC. *JINST* **15**(08), C08022 (2020). doi: [10.1088/1748-0221/15/08/C08022](https://doi.org/10.1088/1748-0221/15/08/C08022)
- [41] L. Lyu, H. Yi, L. Duan, Z. Zhang, and Z. Xiao, Simulation and prototype testing of multi-wire drift chamber arrays for the CEE. *Nucl. Sci. Tech.* **31**(1), 11 (2020). doi: [10.1007/s41365-019-0716-x](https://doi.org/10.1007/s41365-019-0716-x)
- [42] S. H. Zhu *et al.*, Prototype design of readout electronics for Zero Degree Calorimeter in the HIRFL-CSR external-target experiment. *JINST* **16**(08), P08014 (2021). doi: [10.1088/1748-0221/16/08/P08014](https://doi.org/10.1088/1748-0221/16/08/P08014)
- [43] Saint-Gobain, BC-408 material. <https://www.crystals.saint-gobain.com/radiation-detection-scintillators/plastic-scintillators/bc400-bc404-bc408-bc412-bc416>
- [44] J. Adams *et al.*, The STAR Event Plane Detector. *Nucl. Instrum. Meth. A* **968**, 163970 (2020). doi: [10.1016/j.nima.2020.163970](https://doi.org/10.1016/j.nima.2020.163970)
- [45] J. Aichelin, 'Quantum' molecular dynamics: A Dynamical microscopic n-body approach to investigate fragment formation and the nuclear equation of state in heavy-ion collisions. *Phys. Rept.* **202**, 233-360 (1991). doi: [10.1016/0370-1573\(91\)90094-3](https://doi.org/10.1016/0370-1573(91)90094-3)
- [46] R. Brun *et al.*, GEANT detector description and simulation Tool. (1994). doi: [10.17181/CERN.MUHF.DMJ1](https://doi.org/10.17181/CERN.MUHF.DMJ1)
- [47] A. M. Poskanzer and S. A. Voloshin, Methods for analyzing anisotropic flow in relativistic nuclear collisions. *Phys. Rev. C* **58**, 1671-1678 (1998). doi: [10.1103/PhysRevC.58.1671](https://doi.org/10.1103/PhysRevC.58.1671)
- [48] M. Ding *et al.*, Calibration of the DAMPE plastic scintillator detector and its on-orbit performance. *Res. Astron. Astrophys.* **19**(3), 047 (2019). doi: [10.1088/1674-4527/19/3/47](https://doi.org/10.1088/1674-4527/19/3/47)

- [49] J. Adamczewski-Musch *et al.*, Directed, elliptic, and higher order flow harmonics of protons, deuterons, and tritons in Au + Au collisions at $\sqrt{s_{NN}} = 2.4$ GeV. Phys. Rev. Lett. **125**, 262301 (2020). doi: [10.1103/PhysRevLett.125.262301](https://doi.org/10.1103/PhysRevLett.125.262301)
- [50] M. S. Abdallah *et al.*, Light nuclei collectivity from $\sqrt{s_{NN}} = 3$ GeV Au+Au collisions at RHIC. Phys. Lett. B **827**, 136941 (2022). doi: [10.1016/j.physletb.2022.136941](https://doi.org/10.1016/j.physletb.2022.136941)
- [51] P. Russotto *et al.*, Flow probe of symmetry energy in relativistic heavy-ion reactions. Eur. Phys. J. A, **50**, 38 (2014). doi: [10.1140/epja/i2014-14038-5](https://doi.org/10.1140/epja/i2014-14038-5)
- [52] M. Wang *et al.*, Number-of-constituent-quark scaling of elliptic flow: a quantitative study. Nucl. Sci. Tech. **33**, 37 (2022). doi:[10.1007/s41365-022-01019-9](https://doi.org/10.1007/s41365-022-01019-9)
- [53] J. Steinheimer *et al.*, Hypernuclei, dibaryon and antinuclei production in high energy heavy-ion collisions: Thermal production versus Coalescence. Phys. Lett. B **714**, 85-91 (2012). doi: [10.1016/j.physletb.2012.06.069](https://doi.org/10.1016/j.physletb.2012.06.069)
- [54] T.T. Wang and Y. G. Ma, Nucleon-number scalings of anisotropic flows and nuclear modification factor for light nuclei in the squeeze-out region. Eur. Phys. J. A **55**, 102 (2019). doi:[10.1140/epja/i2019-12788-0](https://doi.org/10.1140/epja/i2019-12788-0)
- [55] T.Z. Yan *et al.*, Scaling of anisotropic flow and momentum-space densities for light particles in intermediate energy heavy ion collisions. Phys. Lett. B **638**, 50-54 (2006). doi:[10.1016/j.physletb.2006.05.018](https://doi.org/10.1016/j.physletb.2006.05.018)
- [56] L.M. Fang, Y.G. Ma and S. Zhang, Simulation of collective flow of protons and deuterons in Au+Au collisions at $E_{beam}=1.23A$ GeV with the isospin-dependent quantum molecular dynamics model. Phys. Rev. C **107**, 044904 (2023). doi:[10.1103/PhysRevC.107.044904](https://doi.org/10.1103/PhysRevC.107.044904)